# Compressed Sensing of Monostatic and Multistatic SAR

Ivana Stojanovic, *Member, IEEE*, Müjdat Çetin, *Senior Member, IEEE*, and W. Clem Karl, *Senior Member, IEEE*

***Abstract*—In this letter, we study the impact of compressed data collections from a synthetic aperture radar (SAR) sensor on the reconstruction quality of a scene of interest. Different monostatic and multistatic SAR measurement configurations produce different Fourier sampling patterns. These patterns reflect different spectral and spatial diversity tradeoffs that must be made during task planning. Compressed sensing theory argues that the mutual coherence of the measurement probes is related to the reconstruction performance of sparse domains. With this motivation, we propose a closely related $t_{\%}$-average mutual coherence parameter as a sensing configuration quality parameter and examine its relationship to the reconstruction behavior of various monostatic and ultranarrow-band multistatic configurations. We investigate how this easily computed metric is related to SAR reconstruction quality.**

***Index Terms*—Compressed sensing, multistatic SAR, mutual coherence, synthetic aperture radar (SAR), $t\%$ mutual coherence.**

## I. Introduction

SYNTHETIC aperture radar (SAR) is a remote sensing system capable of producing high-resolution imagery of target scenes independent of time of day, distance, and weather. Conventional SARs are monostatic, with collocated transmit and receive antenna elements. These SAR sensors coherently process multiple sequential observations of a scene under the assumption that the scene is static. Imaging resolution is determined by the bandwidth of the transmitted signals and the size of the synthesized antenna. Greater resolution requires wider bandwidths and larger aspect angles obtained from a longer baseline observation interval. An alternative approach is based on multistatic configurations, wherein spatially dispersed transmitters and receivers sense the scene. Such configurations provide the opportunity for spatial as well as frequency diversity and offer potential advantages in flexible sensor planning, sensing time reduction, and jamming robustness.

To exploit the promise of multistatic sensing, robust methods of reconstructing imagery obtained from general multistatic configurations are needed, as well as tools to understand and evaluate the performance of various sensor configuration choices in a straightforward tractable manner. Recently, the area known as compressed sensing (CS) [1], [2] has received much attention in the signal processing field. CS seeks to acquire as few measurements as possible about an unknown signal and, given these measurements, reconstruct the signal either exactly or with provably small probability of error. The reconstruction methods used in CS are related to sparsity-constrained regularization. Signal reconstruction accuracy is shown to be related to the mutual coherence of the corresponding measurement operator [3], [4]. Furthermore, the CS literature has demonstrated accurate signal reconstructions from measurement of extremely few but randomly chosen Fourier samples of a signal [2], [5]. Since SAR can be viewed as obtaining samples of the spatial Fourier transform of the scattering field [6], these results suggest interesting opportunities for SAR sensing.

The use of sparsity-constrained reconstructions for SAR image formation was first presented in [7] although not within the CS framework. More recently, there have been several applications of CS ideas to radar [8]–[10]. The authors in [8] accurately reconstruct a small number of targets on a time–frequency plane by transmitting a sufficiently incoherent pulse and employing the techniques of CS. The authors in [10] propose the use of chirp pulses and pseudorandom sequences for CS with imaging radars. A CS technique for a SAR is also discussed in [9], where the authors obtain measurements by the random subsampling of a regular aspect–frequency grid in $\mathbf{k}$-space. A SAR CS with reduced number of probes was first discussed in [11] and [12].

In contrast to the previous work, we extend CS treatments to the multistatic scenario and propose a $t_{\%}$-mutual coherence parameter of the measurement operator as a simple measure of sensing configuration quality. Within this framework, we examine different monostatic and ultranarrow-band multistatic configurations, which trade off frequency and geometric diversity. We show how the $t_{\%}$-mutual coherence of the measurement operator is affected by the number of transmitting probes as well as by the number of measurements, and we investigate and demonstrate how this simple metric is related to reconstruction quality.

## II. Multistatic SAR Signal Model

We consider a general multistatic system with spatially distributed transmit and receive antenna elements within a cone positioned at the center of a scene of interest. The scene of interest is modeled by a set of stationary point scatterers reflecting impinging electromagnetic waves isotropically to all receivers within the cone. We introduce a coordinate system with the origin in the center of the area of interest and, for simplicity, model the scene as 2-D (Fig. 1). The relative size of the scene is assumed to be small compared with the distances from the origin of the coordinate system to all transmitters and receivers such that transmit and receive angles would change negligibly if the coordinate origin moved to any point in the scene. Furthermore, we neglect signal propagation attenuation.

Manuscript received November 9, 2012; revised March 24, 2013; accepted April 8, 2013. Date of publication July 9, 2013; date of current version October 10, 2013.

I. Stojanovic is with Boston University, Boston, MA 02215 USA, and also with Scientific Systems Company, Inc., Woburn, MA, 01801 USA.

M. Çetin is with Sabanci University, 80020 Istanbul, Turkey.

W. C. Karl is with Boston University, Boston, MA 02215 USA.

Color versions of one or more of the figures in this paper are available online at http://ieeexplore.ieee.org.

Digital Object Identifier 10.1109/LGRS.2013.2259794

1545-598X © 2013 IEEE

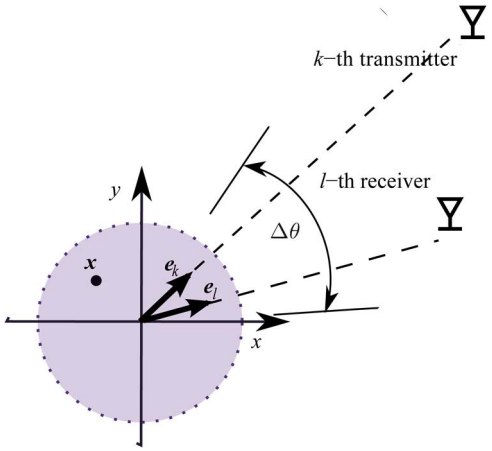


Fig. 1. Geometry of the $kl$th transmit–receive pair with respect to the scene of interest. All transmit and receive pairs are restricted to lie within a cone of the angular extent $\Delta\theta$.

The complex signal received by the $l$th receiver, located at $\mathbf{x}_l = [x_l, y_l]^{\mathrm{T}}$, for the narrow-band excitation from the $k$th transmitter, located at $\mathbf{x}_k = [x_k, y_k]^{\mathrm{T}}$, reflected from a point scatterer at the spatial location $\mathbf{x} = [x, y]^{\mathrm{T}}$ is given by $r_{kl}(t) = s(\mathbf{x})\gamma_k(t - \tau_{kl}(\mathbf{x}))$, where $s(\mathbf{x})$ is the reflectivity of the scatterer, $\gamma_k(t)$ is the transmitted waveform from the $k$th transmitter, and $\tau_{kl}(\mathbf{x})$ is the propagation delay from the transmitter to the scatterer and back from the scatterer to the receiver. The overall received signal from the entire ground patch with radius $L$ is then modeled as a superposition of the returns from all the scattering centers. For narrow-band waveforms, defined by $\gamma_k(t) = \tilde{\gamma}_k(t)e^{j\omega_k t}$, where $\tilde{\gamma}_k(t)$ is a low-pass slowly varying signal and $\omega_k$ is the carrier frequency, the received signal is given by

$$r_{kl}(t) = \int\limits_{\|\mathbf{x}\|_2 \le L} s(\mathbf{x}) e^{j\omega_k(t-\tau_{kl}(\mathbf{x}))} \tilde{\gamma}_k\left(t - \tau_{kl}(\mathbf{x})\right) d\mathbf{x}. \quad (1)$$

In the far-field case, when $\|\mathbf{x}\|_2 \ll \|\mathbf{x}_k\|_2$, $\|\mathbf{x}\|_2 \ll \|\mathbf{x}_l\|_2$, $\omega_k/c\|\mathbf{x}\|_2^2 \ll \|\mathbf{x}_k\|_2$, and $\omega_k/c\|\mathbf{x}\|_2^2 \ll \|\mathbf{x}_l\|_2$, we can use the first-order Taylor series expansion to approximate the propagation delay $\tau_{kl}(\mathbf{x})$ as

$$\tau_{kl}(\mathbf{x}) = \frac{1}{c}\left(\|\mathbf{x}_k - \mathbf{x}\|_2 + \|\mathbf{x}_l - \mathbf{x}\|_2\right) \approx \tau_{kl}(\mathbf{0}) - \frac{1}{c}\mathbf{x}^T\mathbf{e}_{kl}$$

where $\tau_{kl}(\mathbf{0}) \doteq (\|\mathbf{x}_k\|_2 + \|\mathbf{x}_l\|_2)/c$ is the known transmitter–origin–receiver propagation delay and $\mathbf{e}_{kl} \doteq \mathbf{e}_k + \mathbf{e}_l$ is the $kl$th transmit–receiver pair's bistatic range vector. The vectors $\mathbf{e}_k \doteq [\cos\phi_k, \sin\phi_k]^{\mathrm{T}}$ and $\mathbf{e}_l \doteq [\cos\phi_l, \sin\phi_l]^{\mathrm{T}}$ are unit vectors in the direction of the $k$th transmitter and $l$th receiver, respectively.

The chirp signal is the most commonly used spotlight SAR pulse [6], given by $\gamma_k(t) = e^{j\alpha_k t^2} \cdot e^{j\omega_k t}$, $-\tau_c/2 \le t \le \tau_c/2$, where $\omega_k$ is the center frequency and $2\alpha_k$ is the so-called chirp rate of the $k$th transmit element. The narrow-band assumption is satisfied by choosing the chirp-signal parameters such that $2\pi B_k/\omega_k \ll 1$. Ultranarrow-band waveforms are special cases of the chirp signal obtained by setting $\alpha_k = 0$.

We use a general transmitted chirp signal in (1), along with the far-field delay approximation, and apply typical demodulation and baseband processing [6] to obtain the following observed signal model:

$$r_{kl}(t) \approx \int\limits_{\|\mathbf{x}\|_2 < L} s(\mathbf{x}) e^{j\Omega_{kl}(t)\mathbf{x}^{\mathrm{T}}\mathbf{e}_{kl}} d\mathbf{x} \quad (2)$$

where $\Omega_{kl}(t) = (1/c)[\omega_k - 2\alpha_k(t - \tau_{kl}(\mathbf{0}))]$ depends on the frequency content of the transmitted waveform.

The received signal model for the monostatic configuration corresponds to collocated transmit–receiver pairs, and for isotropic pointlike scattering, it is a special case of the multistatic model obtained by setting $\mathbf{x}_k = \mathbf{x}_l$. Note that in a general case, the nature of scattering is different for monostatic and multistatic collection scenarios. The radar collects energy backscattered from a target in the direction of incoming electromagnetic waves in the monostatic case, whereas the backscattered signal is measured in the direction of the receiver in the multistatic case.

## III. CS SAR

CS enables the reconstruction of sparse or compressible signals from a small set of linear nonadaptive measurements, much smaller in size than required by the Nyquist–Shannon theorem [1], [2]. With high probability, accurate reconstructions can be obtained by sparsity-enforcing optimization techniques provided that the signal's sparsifying basis and the random measurement basis are sufficiently incoherent.

According to (2), SAR data represent Fourier $\mathbf{k}$-space measurements of the underlying spatial reflectivity field. Different monostatic and multistatic SAR measurement configurations produce different Fourier sampling patterns. These patterns reflect different spectral and spatial tradeoffs that must be made during task planning. CS theory argues that random Fourier measurements represent good projections for the compressive sampling of pointlike signals [2]. This suggests a natural application to the sparse aperture SAR sensing problem and opens a question of how different monostatic and multistatic SAR sensing configuration constraints influence reconstruction quality for a fixed number of measurements. Furthermore, we are interested in a simple goodness measure that can predict configuration quality before sensing even takes place. Such a quality predictor would allow better task planning and resource utilization. From CS, we know that the mutual coherence of the measurement probes is related to the worst-case reconstruction performance of sparse domains [3], [4]. With this motivation, we examine the relationship of the sensing geometry and a closely related parameter we term the $t_{\%}$-average mutual coherence, as this parameter is expected to provide a better measure of the average reconstruction quality than the mutual coherence which is a pessimistic measure.

In the following, we first describe reduced data collections with nonconventional SAR $\mathbf{k}$-space sampling patterns. Next, we describe the sparsity-enforcing reconstruction and define the $t_{\%}$-average mutual coherence parameter used for the *a priori* evaluation of such sensing configurations.

### A. Sampling Configurations

*1) Monostatic SAR:* One approach to reduced data collection is to directly reduce the number of transmitted probes with regular or random interrupts in the synthetic aperture.

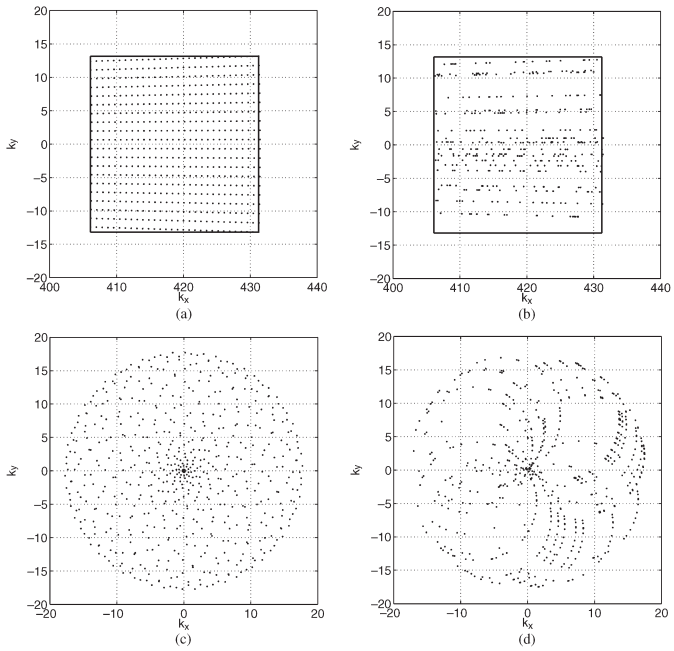


Fig. 2. (a), (b) Monostatic SAR **k**-space sampling patterns for a fixed **k**-space extent. (c), (d) Multistatic **k**-space sampling patterns for circular ultranarrow-band SAR operator. (a) Regular aspect–frequency sampling. (b) Random aspect, random frequency sampling. (c) Regular transmitter-receiver aspect positioning. (d) Random transmitter, random receiver aspect positioning.

We consider regular and random observation sampling patterns within a fixed observation extent $\Delta\Theta$ coupled with regular and random frequency sampling within a desired chirp-signal bandwidth $B$. We do not constrain random aspect/frequency samples to fall on a regular rectangular grid. Fig. 2(a) illustrates the **k**-space sampling pattern when both aspect and frequency are sampled regularly, and Fig. 2(b) illustrates a realization of a **k**-space sampling pattern when both aspect and frequency are sampled randomly.

*2) Multistatic SAR:* Multistatic SAR offers the possibility of different **k**-space sampling patterns with tradeoffs in temporal frequency and spatial transmit/receiver location diversity. In the monostatic case, the chirp-signal bandwidth allowed for the extended coverage of the **k**-space in the range direction. However, in the multistatic case, extended **k**-space coverage can also be achieved with ultranarrow-band signals provided there is a spatial diversity of transmitter and receiver locations. Here, we consider a circular multistatic SAR with continuous-wave ultranarrow-band signal transmission. For the general multistatic SAR, the total number of measurements is calculated as $M = N_{tx}N_{rx}N_f$, where $N_{tx}$ is the number of transmitters/transmitted probes, $N_{rx}$ is the number of receivers, and $N_f$ is the number of frequency samples. In the case of the ultranarrow-band transmission, we have $N_f = 1$ and different sampling patterns are achieved by varying transmitter and receiver angular locations. Fig. 2(c) illustrates the **k**-space sampling pattern when both transmitter and receiver angular locations are sampled regularly, and Fig. 2(d) illustrates a realization of **k**-space sampling when both transmitter and receiver locations are sampled randomly.

### B. Sparse Reconstruction

We consider the image formation of target scenes consisting of a sparse set of point reflectors. The spatial reflectivity is reconstructed on a rectangular grid, resulting in the linear discrete-data SAR model

$$\mathbf{r} = \tilde{\mathbf{\Phi}}\mathbf{s} + \mathbf{n} \tag{3}$$

where $\mathbf{s}$ is the unknown spatial reflectivity vector and $\tilde{\mathbf{\Phi}}$ is derived by discretizing (2). The vector $\mathbf{r}$ represents the observed, thus known, set of return signals at all receivers across time. Its elements are indexed by the tuple $(k, l, t_s)$, with $t_s$ being the sampling times associated with the $kl$th transmit–receive pair, and the spatial frequency $\Omega_{kl}(t)$ and aspect-vector samples $\mathbf{e}_{kl}$ are determined from the sampling configuration requirements.

Both the observed SAR data $\mathbf{r}$ and the underlying scattering field $\mathbf{s}$ are complex valued. In SAR applications, reflectivity magnitudes are of primary interest. We apply sparsity-enforcing regularization directly on the magnitudes of the complex reflectivity field $\mathbf{s}$. In particular, we define the reduced data SAR reconstruction problem as

$$\widehat{\mathbf{s}} = \arg\min_{\mathbf{s}} \|\mathbf{s}\|_1^1 \quad \text{s.t.} \quad \|\mathbf{r} - \tilde{\mathbf{\Phi}}\mathbf{s}\|_2 \leq \sigma \tag{4}$$

where $\sigma$ represents the regularization parameter, $\|\mathbf{s}\|_1^1 = \sum_i \sqrt{(\mathrm{Re}\{\mathbf{s}_i\})^2 + (\mathrm{Im}\{\mathbf{s}_i\})^2}$, $\mathbf{s}_i$ is the $i$th element of the vector $\mathbf{s}$, and $\|\cdot\|_2$ represents the $l_2$-norm. We solve the optimization problem (4) using the software described in [13].

### C. $t\%$-Average Mutual Coherence

The mutual coherence of a measurement operator was discussed as a simple but conservative measure of the ability of sparsity-enforcing reconstruction to accurately reconstruct a signal [3], [4]. In the case of complex $\tilde{\mathbf{\Phi}}$, the mutual coherence of a sensing geometry is defined as

$$\mu(\tilde{\mathbf{\Phi}}) = \max_{i \neq j} g_{ij}, \qquad g_{ij} = \frac{|\langle \phi_i, \phi_j \rangle|}{\|\phi_i\|_2 \|\phi_j\|_2}, i \neq j \tag{5}$$

where $\phi_i$ is the $i$th column of the matrix $\tilde{\mathbf{\Phi}}$ and the inner product is defined as $\langle \phi_i, \phi_j \rangle = \phi_i^H \phi_j$. The $i$th column vector $\phi_i$ can be viewed as a range-aspect "steering vector" of a sensing geometry or a contribution of a scatterer at a specific spatial location to the received phase-history signal. The mutual coherence measures the worst-case correlation between the responses of two distinct spatially distributed reflectors. A less conservative measure connected to average reconstruction performance was proposed in [14] for CS projection optimization. The $t$-average mutual coherence was defined as the average value of the set $\{g_{ij} | g_{ij} > t\}$. In contrast to the $t$-average mutual coherence, we propose to use the $t_{\%}$-average mutual coherence as a measure more closely related to the average reconstruction performance of (4). We define the $t_{\%}$-average mutual coherence, namely, $\mu_{t_{\%}}$, as follows. Let $\mathcal{E}_{t_{\%}}$ be the set of the $t_{\%}$ percent of the largest column cross-correlations $g_{ij}$. The $t_{\%}$-average mutual coherence is defined as

$$\mu_{t_{\%}}(\tilde{\mathbf{\Phi}}) = \frac{\sum_{i \neq j} g_{ij} \mathcal{I}_{ij}(t_{\%})}{\sum_{i \neq j} \mathcal{I}_{ij}(t_{\%})}, \quad \mathcal{I}_{ij}(t_{\%}) = \begin{cases} 1, & g_{ij} \in \mathcal{E}_{t_{\%}} \\ 0, & \text{otherwise.} \end{cases} \tag{6}$$

In other words, $\mu_{t_{\%}}(\tilde{\mathbf{\Phi}})$ measures an average cross-correlation value in a set of the $t_{\%}$ most similar column pairs. The parameter $t_{\%}$ should have a small value in order to accurately represent the tail of the column cross-correlation distribution. This measure is more robust to outliers, which can unfairly dominate the mutual coherence. A large value of $\mu_{t_{\%}}(\tilde{\mathbf{\Phi}})$

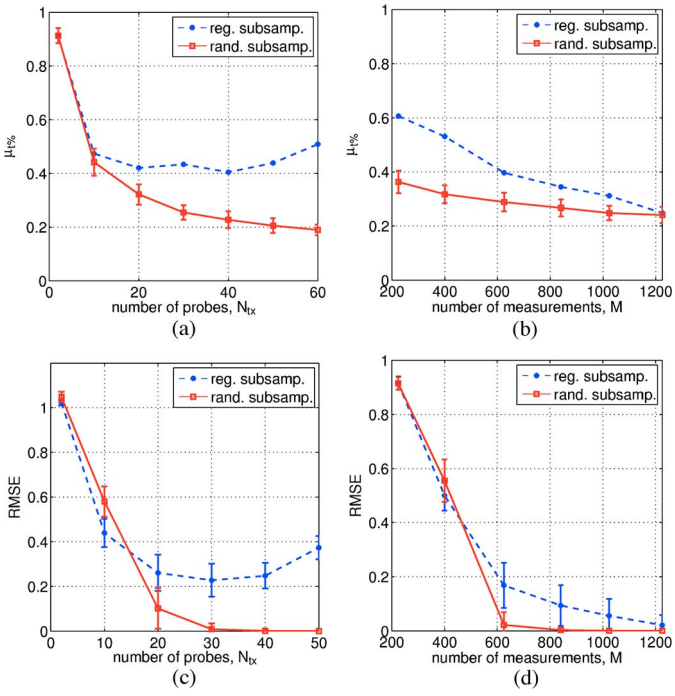


Fig. 3. Monostatic SAR when the ground scene consists of $T = 140$ scatterers. (a), (c) Performance versus sensing configuration for the fixed number of measurements $M = 600$. (b), (d) Performance versus number of measurements $M$ for sensing configurations with $N_{tx} = N_f$. (a), (b) $t_{\%}$-average mutual coherence $\mu_{0.5\%}$. (c), (d) RMSE.

indicates a large number of similar columns of $\tilde{\mathbf{\Phi}}$ that can potentially confuse the reconstruction algorithm.

## IV. Simulations

In this section, we present simulation results averaged over 100 Monte Carlo runs when $\mathbf{n} = 0$ in (3). For regular sampling, we average over different ground-truth scene realizations. In cases that involve random sampling, we average over different SAR operator and ground-scene realizations. For each realization of $\tilde{\mathbf{\Phi}}$, we measure the $t_{\%}$-average mutual coherence $\mu_{t_{\%}}(\tilde{\mathbf{\Phi}})$, for $t_{\%} = 0.5\%$, and display its average over all Monte Carlo runs. The ground-truth scene consists of $T$ randomly dispersed scatterers each with unit magnitude and random phase uniformly distributed in the range $[0, 2\pi]$. Reconstruction performance is measured through the relative mean square error (RMSE), defined as $RMSE = E[\|\widehat{\mathbf{s}} - \mathbf{s}_0\|_2 / \|\mathbf{s}_0\|_2]$, where $\mathbf{s}_0$ is the ground truth signal, $\widehat{\mathbf{s}}$ is its estimate from a reduced set of measurements, and $E[\cdot]$ stands for an empirical average over Monte Carlo runs.

*1) Simulation Results for Monostatic CS SAR:* We consider the monostatic spotlight SAR imaging of a small ground patch of size $(D_x, D_y) = (10, 10)$ m when observed over a narrow-angle aspect cone of $\Delta\theta = 3.5°$. The transmitted waveforms are chirp signals with $f_o = 10$ GHz and $B = 600$ MHz. The nominal range resolution is $\rho_x = c/(2B) = .25$ m, and the nominal cross-range resolution is $\rho_y = \lambda/(4\sin(\Delta\theta/2)) = 0.25$ m. Assuming that the pixel spacing matches the nominal resolution, we seek to reconstruct a $40 \times 40$ pixel reflectivity image.

In Fig. 3, we show the results when the ground scene consists of $T = 140$ randomly dispersed nonzero scatterers. The left column shows the results at the fixed number of measurements $M = N_{tx}N_f = 600$ as we vary the number of transmitted probes $N_{tx}$. The right column shows the results as a function of the number of measurements $M$ for sensing configurations with equal numbers of frequency and aspect samples, i.e., $N_{tx} = N_f$. Comparing the $\mu_{t_{\%}}$ curves to the RMSE curves, we see that as the $t_{\%}$-average mutual coherence is lowered, the reconstruction quality improves. Regular sampling introduces signal aliasing manifested as periodic and large-column cross-correlation peaks that confuse the reconstruction algorithm. The $t_{\%}$-average mutual coherence is the lowest when $\mathbf{k}$-space sampling points cover the available $\mathbf{k}$-space extent most uniformly. The most uniform coverage in the regular subsampling case is achieved when the ratio of the number of aspect angles to the number of frequency samples is approximately $N_{tx}/N_f = \Delta K_x/\Delta K_y$, where $\Delta K_x(\Delta K_y)$ is the $\mathbf{k}$-space extent in the cross-range (range) direction. On the other hand, in the random sampling case, the $\mathbf{k}$-space coverage becomes more uniform as the number of transmitted probes increases. This is reflected in the lower values of the $\mu_{t_{\%}}$. We see that increasing the number of transmitted probes after a certain value of $\mu_{t_{\%}}$ is reached has only a small impact on the reconstruction performance. Finally, the monostatic random sensing enables high-quality reconstructions with a smaller number of probes $(N_{tx} \geq 25)$ than required by the conventional SAR Nyquist sampling where $N_{tx} = 40$.

*2) Simulation Results for Multistatic CS SAR:* The main advantage of CS in the monostatic scenario is the reduction of data storage and reduction in the number of transmitted probes. Data collection time cannot be reduced, as the monostatic SAR platform covers the whole aspect range sequentially in time. On the other hand, multistatic SAR has the potential to further reduce the data acquisition time through the use of a multitude of spatially dispersed transmitters and receivers. Theoretically, there exist many multistatic geometries with similar $\mathbf{k}$-space coverage as in the monostatic case and, thus, similar reconstruction results in the case of isotropic scattering. In an extreme case, we consider ultranarrow-band circular multistatic configurations with $N_f = 1$ and transmitters and receivers placed around the scene in a full circle [15].

In order to carry out simulations comparable with the monostatic case, the carrier wavelength is reduced such that spatial resolutions of the two configurations are approximately the same. In our simulations, each transmitter sends out an ultranarrow-band waveform signal with a frequency that satisfies $\rho_x = \rho_y = 0.25 = \sqrt{2}c/(4f_o)$. The scene size is the same as in the monostatic simulation cases. We assume that the isotropic scattering assumption is valid for the circular multistatic configuration. When this assumption is violated, sparsity-driven imaging techniques that take the anisotropic nature of the scattering into account can be used (e.g., [16]), and the reconstruction quality metrics may need to be modified.

In Fig. 4, we show the results as a function of the number of spatially dispersed transmitters $N_{tx}$ when the total number of measurements is held fixed to $M = 600 = N_{tx}N_{rx}N_f$ and the signal support size is $T = 140$. All sampling cases result in a $\mathbf{k}$-space pattern that deviates significantly from a regular $\mathbf{k}$-grid. This translates into a significantly reduced coherence of configurations with a few transmitted probes and higher reconstruction quality as compared with the monostatic case with the same number of transmitted probes. Furthermore, different multistatic sampling patterns achieve similar performance. While random sampling was the key to the improved performance in the monostatic case, circular multistatic configuration is robust to transmit/receive sensor aspects.

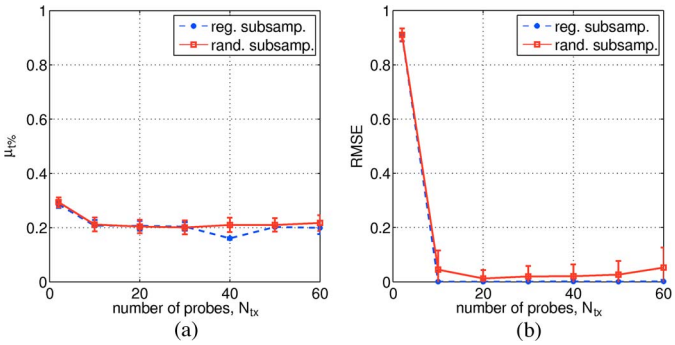


Fig. 4. Multistatic ultranarrow-band SAR performance versus sensing configuration for fixed $M = 600$ and $T = 140$. (a) $\mu_{0.5\%}$. (b) RMSE.

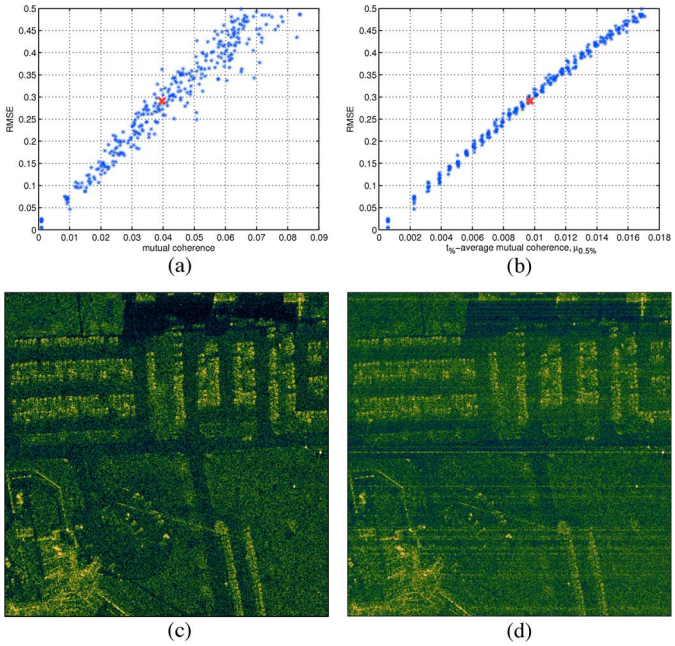


Fig. 5. GOTCHA SAR examples. (a) RMSE versus mutual coherence. (b) RMSE versus $\mu_{0.5\%}$. (c) Sample reconstruction corresponding to the red $\times$ point in (a) and (b) (i.e., $\mu \approx 0.04$ and $\mu_{0.5\%} \approx 0.01$). (d) Matched filter reconstruction corresponding to (c).

*3) Results Using GOTCHA SAR Imagery:* In this section, we compare the utility of $t_{\%}$-average and conventional mutual coherence using the publicly released GOTCHA SAR data set [17]. Starting with the complete phase history data of a $1024 \times 1024$-pixel image from this data set, we generate incomplete data by randomly deleting individual probes while keeping all frequency samples of retained probes. We use $\sigma = 0.1$ and set the maximum number of iterations to 200 when solving (4). In Fig. 5(a) and (b), we show the scatter plots of RMSE versus mutual coherence and RMSE versus $\mu_{0.5\%}$-average mutual coherence obtained using ten Monte Carlo realizations of incomplete data when the total number of interrupts is $1 + 16i, i = 1, \ldots, 31$. We see that the RMSE variance at any particular value of $\mu_{0.5\%}$ is much smaller than the RMSE variance at any particular value of the mutual coherence, implying that $\mu_{0.5\%}$ is a better predictor of reconstruction quality than mutual coherence. A sample reconstruction from the data containing 240 random synthetic aperture gaps is shown in Fig. 5(c). The corresponding matched filter reconstruction is shown in Fig. 5(d). We see that leakage artifacts due to reduced data are successfully removed with sparse reconstruction using (4).

## V. Conclusion

In this letter, we have studied different monostatic and multistatic SAR measurement configurations in the context of CS. We have shown that reconstructions of similar quality can be obtained using either the wide-band monostatic or ultranarrow-band multistatic configurations, effectively trading off frequency for geometric diversity. In both cases, configurations with sufficiently small values of the $t_{\%}$-average mutual coherence achieve high-quality reconstruction performance. The $t_{\%}$-average mutual coherence is an easily computed parameter that can be used in the real-time design or evaluation of sensing configurations for, e.g., the task planning of multimode radars. In the multistatic case, it is straightforward to obtain low coherence either by regular or random transmit/receive aspect sampling, whereas in the monostatic case, randomness in the sampling pattern leads to lower coherence. In the monostatic case, CS and sparsity-driven reconstruction allow for reduced onboard data storage and sensing with a reduced number of transmitted probes relative to what is conventionally required. In the multistatic case, CS and sparsity-driven reconstruction allow for sensing with fewer transmitted probes but also reduced acquisition time when compared with the monostatic case.

## References

[1] D. L. Donoho, "Compressed sensing," *IEEE Trans. Inf. Theory*, vol. 52, no. 4, pp. 1289–1306, Apr. 2006.
[2] E. Candes, J. Romberg, and T. Tao, "Robust uncertainty principles: Exact signal reconstruction from highly incomplete frequency information," *IEEE Trans. Inf. Theory*, vol. 52, no. 2, pp. 489–509, Feb. 2006.
[3] E. Candes and J. Romberg, "Sparsity and incoherence in compressive sampling," *Inverse Probl.*, vol. 23, no. 3, pp. 969–985, Jun. 2007.
[4] D. Donoho and X. Huo, "Uncertainty principles and ideal atomic decomposition," *IEEE Trans. Inf. Theory*, vol. 47, no. 7, pp. 2845–2862, Nov. 2001.
[5] M. Lustig, D. L. Donoho, and J. M. Pauly, "Sparse MRI: The application of compressed sensing for rapid MR imaging," *Magn. Resonance Med.*, vol. 58, no. 6, pp. 1182–1195, Dec. 2007.
[6] C. V. Jakowatz, D. E. Wahl, P. S. Eichel, D. C. Ghiglian, and P. A. Thompson, *Spotlight-mode Synthetic Aperture Radar: A Signal Processing Approach*. Norwell, MA, USA: Kluwer, 1996.
[7] M. Çetin, "Feature-enhanced synthetic aperture radar imaging," Ph.D. dissertation, Boston Univ., Boston, MA, USA, 2001.
[8] M. Herman and T. Strohmer, "High-resolution radar via compressed sensing," *IEEE Trans. Signal Process.*, vol. 57, no. 6, pp. 2275–2284, Jun. 2009.
[9] Y.-S. Yoon and M. G. Amin, "Compressed sensing technique for high-resolution radar imaging," *Signal Process., Sensor Fusion, Target Recog. XVII, SPIE*, vol. 6968, no. 1, pp. 69681A-1–69681A-10, 2008.
[10] R. Baraniuk and P. Steeghs, "Compressive radar imaging," in *Proc. IEEE Radar Conf.*, 2007, pp. 128–133.
[11] I. Stojanovic, W. C. Karl, and M. Çetin, "Compressed sensing of monostatic and multi-static SAR," *Algorithms Synthetic Aperture Radar Imagery XVI*, ser. Proc. SPIE, vol. 7337, pp. 733 705-1–733 705-1, Apr. 2009.
[12] V. Patel, G. Easley, D. Healy, and R. Chellappa, "Compressed synthetic aperture radar," *IEEE J. Sel. Topics Signal Process.*, vol. 4, no. 2, pp. 244–254, Apr. 2010.
[13] E. van den Berg and M. P. Friedlander, SPGL1: A solver for large-scale sparse reconstruction, Jun. 2007. [Online]. Available: http://www.cs.ubc.ca/labs/scl/spgl1
[14] M. Elad, "Optimized projections for compressed sensing," *IEEE Trans. Signal Process.*, vol. 55, no. 12, pp. 5695–5702, Dec. 2007.
[15] B. Himed, H. Bascom, J. Clancy, and M. C. Wicks, "Tomography of moving targets (TMT)," in *Proc. SPIE, Sensors, Syst., Next-Gener. Satell. V*, H. Fujisada, J. B. Lurie, and K. Weber, Eds., Toulouse, France, 2001, vol. 4540, no. 1, pp. 608–619.
[16] I. Stojanovic, M. Çetin, and W. C. Karl, "Joint space aspect reconstruction of wide-angle SAR exploiting sparsity," *Proc. SPIE: Algorithms Synthetic Aperture Radar Imagery XV*, vol. 6970, pp. 697005-1–697005-12, May 2008.
[17] S. M. Scarborough, L. Gorham, M. J. Minardi, U. K. Majumder, M. G. Judge, L. Moore, L. Novak, S. Jaroszewksi, and A. Pieramico, *A challenge problem for SAR change detection and data compression*, ser. Proc. SPIE, vol. 7699, pp. 769 90U-1–769 90U-5, Apr. 2010.